Monthly Notices of the ROYAL ASTRONOMICAL SOCIETY

MNRAS **548,** 1–12 (2026)
Advance Access publication 2026 April 15

https://doi.org/10.1093/mnras/stag714

Investigating the circumgalactic medium through Mg II absorption coincidence

Paryag Sharma [1★] Raghunathan Srianand [2] Hum Chand [1] and Labanya Kumar Guha [3]

[1] *Department of Physics and Astronomical Science, Central University of Himachal Pradesh, Dharamshala 176215, India*
[2] *Inter-University Centre for Astronomy and Astrophysics, Post Bag 4, Ganeshkhind, Pune 411 007, India*
[3] *Indian Institute of Astrophysics, II Block, Koramangala, Bengaluru-560 034, India*

Accepted 2026 April 13. Received 2026 March 30; in original form 2026 January 7

ABSTRACT

We present a statistical measurement of the transverse coherence of Mg II λλ2796, 2803 absorption using a large sample of 9204 absorber-centric quasar sightline pairs from the Sloan Digital Sky Survey. We quantify the probability that an Mg II absorber detected along one sightline is also present along a nearby sightline, and measure how this coincidence probability varies with projected separation from ∼50 kpc to ∼1 Mpc. The resulting coincidence curve exhibits a clear two-regime structure: the coincidence probability rises steeply to ∼5–8 per cent at separations below ∼100 kpc, but declines rapidly beyond this scale and settles into a low plateau of ∼1–2 per cent out to ∼1 Mpc. A simple geometrical single-halo model reproduces the enhanced probability at $\lesssim$100 kpc, while the large-scale plateau is well explained by the expected contribution from galaxy clustering, confirmed using both photometric galaxy counts and the two-point correlation function. A complementary stacking analysis reveals a significant excess in Mg II equivalent width in paired sightlines lacking individual detections, implying a coherence scale of ∼100–200 kpc for the cool, metal-enriched CGM. Together, these results identify the transition from a halo-dominated coherence regime at small separations to a clustering-dominated regime at large scales, bridging the gap between small-scale lensing constraints and megaparsec-scale absorber clustering studies.

Key words: galaxies: haloes – quasars: absorption lines – quasars: general.

1 INTRODUCTION

Since the earliest quasar spectra were recorded, intervening metal absorption lines have revealed the presence of diffuse, ionized and metal enriched gas along the line of sight (J. E. Gunn & B. A. Peterson 1965; A. Sandage 1965; E. M. Burbidge, C. R. Lynds & G. R. Burbidge 1966; E. M. Burbidge 1967). Subsequent surveys established that many of these absorbers arise from foreground galaxies intersecting quasar sightlines at small impact parameters[1] (denoted by b; J. Bergeron & P. Boissé 1991; C. C. Steidel 1995). Among these systems, absorption by the Mg II λλ2796, 2803 doublet has become one of the most widely used tracers of cool, metal-enriched gas associated with the extended circumgalactic medium (CGM) of low-z (i.e. $z < 1.0$) galaxies. In particular, it traces the low ionization (i.e. neutral or singly ionized), low temperature (i.e. $T \sim 10^4$ K) gas with typically high H I column density (i.e. log N(H I) $\geq$ 17), and serves as a key diagnostic of the physical conditions in the CGM (e.g. R. Srianand & P. Khare 1994). The CGM plays a central role in galaxy evolution by mediating the inflow, outflow, cooling, and recycling of baryons, and Mg II absorbers provide an effective means to probe these processes over cosmic time (J. Tumlinson, M. S. Peeples & J. K. Werk 2017; M. Fumagalli 2024; C. W. Churchill 2025).

Absorption-line spectroscopy of background quasars offers a particularly powerful method for detecting faint CGM gas, as its sensitivity depends primarily on the achievable signal-to-noise ratio rather than the luminosity of the foreground galaxy. However, a single sightline provides a measurement along a pencil-beam through a complex and anisotropic medium, making it difficult to determine the spatial extent, morphology, and coherence scale of Mg II absorbing structures. To overcome this limitation, quasar pairs and multiply imaged gravitationally lensed quasars can be used to sample multiple closely spaced sightlines through the same foreground structures, enabling direct measurements of absorber coincidence and transverse variations. (e.g. see P. Jalan, H. Chand & R. Srianand 2019; P. Sharma et al. 2025).

Using one of the largest samples of quasar pairs available at that time, D. Tytler et al. (2009) showed that the probability of finding a coincident metal absorption system declines steeply with increasing transverse separation – from ∼ 20–50 per cent at $\lesssim$ 200 kpc to $\lesssim$1 per cent at ∼ 1–2 Mpc – consistent with expectations from normal galaxy clustering. Similarly, K. H. R. Rubin et al. (2015) have studied coincidence of optically thick ab-

★ E-mail: panditparyag@gmail.com

[1] Impact parameter is the projected physical separation between the centre of the galaxy and quasar sight line.

sorbers around 40 DLAs at $1.6 \leq z \leq 3.6$ at projected separations $\leq$300 kpc using closely spaced quasar pairs. On the Mpc scale, cross-correlation analysis of C IV absorption along widely spaced quasar sightlines are used to constrain effective absorber bias (e.g. see S. Gontcho A Gontcho et al. 2018).

At much smaller scales, lensed quasars and very close quasar pairs allow tests of the internal coherence of Mg II absorbing structures within individual haloes. Analyses of multi-image lenses show that strong Mg II and damped Lyα absorbers can vary substantially between sightlines separated by a few to a few tens of kpc (e.g. S. L. Ellison et al. 2004; J. A. Rogerson & P. B. Hall 2012; F. S. Zahedy et al. 2016; K. H. R. Rubin et al. 2018; R. Augustin et al. 2021; K. Okoshi et al. 2021), with observed equivalent-width differences implying inhomogeneous structure of the absorbing gas on ∼6–12 kpc scales. J. A. Rogerson & P. B. Hall (2012) compared Mg II equivalent widths across multiple images using Monte Carlo realizations of the halo model (as in J. L. Tinker & H.-W. Chen 2008) and found that the observed sightline-to-sightline scatter requires a very small characteristic coherence length, $\ell_c \simeq 0.5\,h^{-1}$ kpc, along with a moderate covering fraction $f_c \simeq 0.6$. Large coherence scales ($\ell_c \gtrsim 20$ kpc) were strongly disfavoured, indicating that Mg II absorption can fluctuate substantially even over sub-kpc separations. Spatially resolved velocity maps constructed from multi-image spectroscopy further demonstrate coherent kinematic structures (e.g. rotating or accreting streams, collimated outflows) on ∼5–10 kpc scales (H.-W. Chen et al. 2014). More recent tomographic MUSE studies of strongly lensed quasars find that the fractional difference in Mg II equivalent width generally increases with physical separation and suggest a typical coherence scale of order ∼10 kpc for low-ionization gas, while high-ionization phases (e.g. C IV) appear more coherent at the same separations (R. Dutta et al. 2024).

Recent work using gravitational-arc tomography provides a complementary, two-dimensional perspective on absorber structure. Spatially resolved spectroscopy of giant arcs has revealed a clumpy, anisotropic Mg II -bearing medium, with absorption strength declining with projected distance and showing strong azimuthal dependence indicative of disc/flow geometry and patchy covering fractions on kpc scales (S. Lopez et al. 2018; A. Afruni et al. 2023; A. Shaban et al. 2025). In particular, A. Afruni et al. (2023) used VLT/MUSE observations of gravitational arcs to measure the spatial coherence of Mg II absorption across dozens of closely spaced sightlines, finding characteristic coherence scales of order ∼ 1–8 kpc. These results reinforce the picture from lensed-quasar studies that low-ionization gas is inhomogeneous on kiloparsec (and sub-kpc) scales and demonstrate the power of extended background sources for mapping absorber morphology.

Together, these works indicate that Mg II absorption exhibits small-scale clumpiness within halos as well as larger-scale correlations driven by galaxy clustering, motivating a systematic study that quantifies coincidence probabilities as a function of impact parameter, absorber strength and redshift. We also would like to understand the absorber–absorber coincidences on hundred-kpc to Mpc scales in terms of the radial distribution of gas in the CGM and immediate environments of individual galaxies at small scales and galaxy–galaxy clustering at large scales (see for example, J. L. Tinker & H.-W. Chen 2008).

Modern wide-field spectroscopic surveys such as SDSS (B. W. Lyke et al. 2020) provide large samples of quasars spanning the separations necessary to bridge the gap between the sub-kpc lensed-quasar regime and the Mpc-scale clustering regime. This opens the possibility of performing systematic measurements of Mg II absorber coincidence as a function of sightline separations, enabling new constraints on the coherence, covering fraction, and spatial distribution of cool CGM gas. In this work, we exploit a sample of projected quasar pairs with well-characterized sensitivity and equivalent-width limits to measure the coincident Mg II absorption across tens to hundreds of kiloparsecs. By comparing our results with expectations from galaxy clustering and single halo-based models, we aim to constrain the physical scales over which Mg II absorbing gas remains coherent and to characterize at what scale the coincidence probability transitions from the single-halo regime to the large-scale galaxy-clustering regime.

This paper is organized as follows: Section 2 describes our sample and absorption line measurements. Section 3 presents our analysis and results, while Section 4 presents the discussion and conclusions of our findings. Throughout this work, we assume a flat ΛCDM cosmology with $\Omega_m = 0.3$, $\Omega_\Lambda = 0.7$, and $h_0 = 0.7$.

2 SAMPLE AND ABSORPTION LINE MEASUREMENTS

We constructed our sample from the SDSS-DR16Q quasar catalogue (B. W. Lyke et al. 2020), which contains 750 414 quasars. The initial list of Mg II absorbers were gathered from the SDSS DR16 Mg II absorber catalogue from A. Anand, D. Nelson & G. Kauffmann (2021), supplemented with absorbers from G. Zhu & B. Ménard (2013) to improve completeness. Some absorption features that appear closely spaced in wavelength do not correspond to distinct physical systems. Such duplicates arise both from the combination of two independently generated absorber catalogues and from repeated detections of the same system by the automated line-finding pipelines used within each catalogue. To address this, we identified and removed duplicate entries, retaining only unique absorption systems detected at a significance of at least 3σ.

As a starting point we use these absorber catalogs for the detection of Mg II systems along individual quasar sightlines. Each detected Mg II absorber along a sightline is treated as an independent single-sightline case; consequently, a given sightline may contribute multiple such cases if it hosts multiple absorbers. Throughout this work, we refer to these independent absorber-centric quasar sightline cases as 'pairs' such that each case is defined by an absorber and its corresponding companion sightline either with or without absorber. We then constructed a pair sample by requiring that Mg II absorber is detected at least in one sightline, with a projected separation (D) of <1 Mpc at the absorber redshift. This selection resulted in 38 154 pairs. For each pair, we further imposed two conditions: (1) $z_{\rm abs} < z_{\rm qso}$ is satisfied for quasars in both sightlines with a velocity offset greater than 3000 km s^{-1}, and (2) the observed wavelength of the Mg II doublet lies outside the Lyman-α forest region of the companion quasar spectrum. Applying these criteria yielded a final sample of 25 764 pairs.

Automated absorber catalogs are often incomplete and are therefore commonly supplemented by visual inspection. However, given the large size of our sample, visual inspection is impractical and may introduce subjective biases. We therefore adopt a more robust and fully automated approach based on template matching to confirm the catalogue based detection of Mg II absorber in all 25 764 pairs towards both the sightlines. Template matching is a standard technique in which a model absorption profile is cross-correlated with the observed spectrum to enhance the detectability of weak or noisy features (e.g. G.

Zhu & B. Ménard 2013). For this we perform cross-correlation within ± 1500 km s^{-1} around the absorber redshift towards both the sightlines in a pair. A detection was retained only if the maximum correlation peak within the search window exceeded the local mean by at least three times the standard deviation. The corresponding peak position provided an initial estimate of the absorber redshift, which was subsequently refined through Gaussian profile fitting. As an additional consistency check, we verified the doublet nature of Mg II absorption using an auto-correlation test, requiring significant peaks at the expected rest wavelength separation of $\sim$7.18 Å. In case of coincidence, the absorbers may be independently cataloged along both sightlines of a pair within ± 1500 kms^{-1} which can lead to counting the same pair twice. In such cases, we retain only a single entry to avoid duplication. This procedure yielded 19 740 pairs. The equivalent width (W) was measured by integrating the observed normalized flux over a $\pm 3\sigma$ window centred on the fitted line centroid, where σ corresponds to the standard deviation of the best-fitting Gaussian profile to the absorption line. To minimize false positives, we required the Mg II doublet ratio to satisfy $0.7 < W_{2796}/W_{2803} < 2.6$, and the rest-frame full width at half maximum (FWHM) of the line profile to be <5 Å. These criteria lead to 18 618 pairs.

For each pixel, the equivalent width detection limit was computed using a weighted sum of the line spread function, modelled as a Gaussian and integrated over a 10-pixel window centred on the pixel. To define coincidences for a given equivalent-width threshold, both sightlines were required to be sensitive to that threshold at more 3σ level, and each absorber had to exceed the threshold with at least 3σ significance. For non-coincident cases, both sightlines met the 3σ sensitivity criterion, but only one exhibited an absorber above the threshold at $\geq 3\sigma$ significance. For equivalent-width thresholds of 1.0 and 0.6 Å, we identify 71 and 82 coincident pairs out of total samples of 7719 and 5512 quasar pairs, respectively with 4027 pairs common among them. All these details are summarized in Table 1, and the full sample of 9204 unique pairs is listed in Table 2.

Fig. 1 shows the distribution of the rest-frame Mg II equivalent width (W_{2796}) and projected quasar-pair separation (D) as a function of absorber redshift for two equivalent-width thresholds, $W_{2796} > 0.6$ Å (left panels) and $W_{2796} > 1.0$ Å (right panels). Coincident absorbers are highlighted with filled symbols, while non-coincident systems are shown with lighter points. The marginal histograms shown along the top of each panel represent the normalized redshift distributions of the coincident and non-coincident samples, while the histograms along the right-hand side show the normalized distributions of rest-frame equivalent width (top panels) or projected separation (bottom panels). In all cases, the histograms are normalized to unit area to facilitate a direct visual comparison between the two samples, independent of their differing sample sizes. To quantitatively assess whether the coincident and non-coincident systems are drawn from the same underlying distributions, we performed Kolmogorov–Smirnov (KS) tests on both the projected separation and absorber redshift distributions. For the $W_{2796} > 0.6$ Å sample, the KS test yields $p = 0.08$ for the separation distribution and $p = 0.41$ for the redshift distribution. Similarly, for the $W_{2796} > 1.0$ Å sample, we obtain $p = 0.16$ for separation and $p = 0.09$ for redshift. In both cases, the KS tests do not reject the null hypothesis that the coincident and non-coincident samples are drawn from the same parent distributions. This result indicates that the global redshift and separation distributions of coincident absorbers are statistically consistent with those of the non-coincident population. However, this does not preclude a relative excess of coincident absorbers at small projected separations. The KS test is sensitive to differences across the full distribution and may not capture localized enhancements at small D, which are more directly probed by the binned coincidence probabilities and the halo-scale modelling presented in subsequent sections.

Table 1. Summary of sample selection. Counts are reported in terms of 'pairs', where each pair corresponds to an absorber-defined case consisting of one sightline with a detected absorber and its corresponding companion sightline, which may or may not exhibit absorption. Hence, a given quasar sightline may therefore contribute multiple pairs if it hosts multiple absorbers.

S. No.	Selection step	Count
(1)	SDSS-DR16Q quasars	750 414
(2)	The pairs in (1) satisfying $\leq$1000 kpc and an absorber in at least one sightline	38 154
(3)	The pairs in (2) satisfying $z_{\rm abs} < z_{\rm qso}$, $\Delta v > 3000$ km s^{-1}, no Ly α overlap	25 764
(4)	The pairs in (3) satisfying the cross + auto-correlation criteria either in one or both sightlines	19 740
(5)	The pairs in (4) satisfying FWHM < 5 Å, doublet ratio 0.7–2.6 either in one or both sightlines	18 618
	Pairs sample with SNR satisfying for threshold of $W^{\rm th}_{2796} > 1.0$ Å	
(6)	The pairs in (5) with spectra SNR satisfying $W_{2796} > 1.0$ Å in both and absorption either in one or both sightlines	7719
(7)	The pairs in (5) with spectra SNR satisfying $W_{2796} > 1.0$ Å in both and absorption in both sightlines (Coincidence)	71
	Pairs sample with SNR satisfying for threshold of $W^{\rm th}_{2796} > 0.6$ Å	
(8)	The pairs in (5) with spectra SNR satisfying $W_{2796} > 0.6$ Å in both and absorption either in one or both sightlines	5512
(9)	The pairs in (5) with spectra SNR satisfying $W_{2796} > 0.6$ Å in both and absorption in both sightlines (Coincidence)	82

Fig. 2 shows the line-of-sight velocity separations of coincident Mg II absorbers that satisfy the $W_{2796} > 0.6$ Å (left panel) and $W_{2796} > 1.0$ Å (right panel) thresholds as a function of projected separation between the quasar sightlines. Individual points represent the measured velocity offsets, while the larger symbols with horizontal error bars indicate the mean velocity separation in bins of projected separation, with the error bars denoting the corresponding dispersion. Two things are evident from this figure. First, at a given projected separation, the velocity off-set has a small scatter for the strong absorbers at lower projected separation (D). Secondly the spread in velocity off-set increases with increasing projected separation for a given equivalent width cutoff.

Fig. 3 shows the ratio of coincident pairs to total pairs as a function of projected separation (D) at $z_{\rm abs}$ for these two equivalent width thresholds. The uncertainties on the coincidence probabilities were estimated using binomial statistics, corresponding to a 68 per cent (1σ) confidence level. We constructed a control sample by randomly reassigning quasar partners while preserving the absorber redshift and projected separation. The same analysis was repeated on this control sample, and the resulting coincidence probabilities as a function of separation are shown in Fig. 3 for comparison.

Table 2. Our final sample consists of 9204 pairs as summarized in Table 1. Of these, 1485 pairs are used only for the analysis with an equivalent-width threshold of EW $\geq$ 0.6 Å, 3692 pairs are used only for the EW $\geq$ 1.0 Å analysis, and 4027 pairs are common to both samples as listed below. Out of the total 5512 pairs used in the EW $\geq$ 0.6 Å sample, 82 show coincident absorption. Similarly, among the 7719 pairs used in the EW $\geq$ 1.0 Å sample, 71 exhibit coincidence. The *Thresh. Flag* column denotes the equivalent-width threshold satisfied by each system: First sample (S_1) with $W_{2796} > 0.6$ Å, and second sample (S_2) with $W_{2796} > 1.0$ Å, and S_1S_2 (both). The *Coinc. Flag* column indicates whether Mg II absorption satisfying the corresponding threshold is detected in both sightlines (1) or not (0). For non-coincident systems, only the sightline containing detected absorption is listed; columns corresponding to the other sightline without detection are assigned a placeholder value of −999. Only a subset of columns and rows is shown here for illustration; the full table is available online.

QSO$_1$	$Z_{QSO,1}$	QSO$_2$	$Z_{QSO,2}$	D (kpc)	$z_{abs,1}$	$W_{2796,1}$ (Å)	$\sigma_{W,1}$ (Å)	$z_{abs,2}$	$W_{2796,2}$ (Å)	$\sigma_{W,2}$ (Å)	EW$_{lim,1}$ (Å)	EW$_{lim,2}$ (Å)	Thresh. Flag	Coinc. Flag
(1)	(2)	(3)	(4)	(5)	(6)	(7)	(8)	(9)	(10)	(11)	(12)	(13)	(14)	(15)
000014.12−030936.5	1.9768	000016.08−030809.8	1.9821	737.9	−999	−999	−999	1.0299	1.04	0.20	0.0655	0.1049	S1S2	0
000024.62 + 204530.4	1.013	000030.10 + 204617.9	1.2125	701.2	0.8886	1.62	0.42	−999	−999	−999	0.2140	0.1263	S2	0
000036.48 + 321102.4	3.221	000041.24 + 321032.9	1.8672	535.2	−999	−999	−999	0.9721	3.05	0.20	0.2193	0.1278	S2	0
–	–	–	–	–	–	–	–	–	–	–	–	–	–	–

3 RESULTS

The curves shown in Fig. 3 exhibit two distinct regimes: a steep rise in the coincidence probability at $D \lesssim 100$ kpc, followed by a nearly flat plateau at larger separations. At small impact parameters ($D \lesssim 100$ kpc), the observed coincidence probabilities are $0.088^{+0.051}_{-0.033}$ for $W_{2796} > 0.6$ Å and $0.062^{+0.037}_{-0.023}$ for $W_{2796} > 1.0$ Å. This excess at small separations is indicative of absorption arising on halo scales, which we model in the following sections as a single-halo contribution. At larger separations ($D \gtrsim 100$ kpc), the coincidence probability flattens to mean value of 0.0162 ± 0.0053 for $W_{2796} > 0.6$ Å and 0.0087 ± 0.0023 for $W_{2796} > 1.0$ Å, where the quoted uncertainties across radial bins corresponding to a 68 per cent (1σ) confidence level using binomial statistics. In this regime, coincident absorption is dominated by correlated but distinct galaxies tracing the same large-scale structure and is therefore modelled as a clustering-driven contribution. For comparison, the corresponding control samples yield significantly lower mean probabilities of 0.0048 ± 0.0019 and 0.0026 ± 0.0008 for the same equivalent-width thresholds, confirming that the observed plateau reflects genuine clustering rather than chance alignments. We also examine the coincidence probability of our sample without imposing any equivalent-width threshold ($W_{2796} > 0$), retaining only the 3σ detection requirement. In this case, $D < 100$ kpc bin shows a coincidence probability of $0.038^{+0.018}_{-0.012}$, while the average probability at $D > 100$ kpc is 0.0088 ± 0.0025. This confirms the trend found for the equivalent width limited samples. The lower amplitude relative to the equivalent-width-limited samples arises because our sample consists of large number of low SNR spectra where only very strong lines are detectable. These spectra contribute to the denominator without proportionately contribute to the numerator. As a result, the $W_{2796} > 0$ sample should only be treated as a consistency check.

3.1 Modelling coincident probability due to single halo

The rest-frame equivalent width of Mg II absorption is known to anticorrelate with impact parameter (b), though with significant scatter (J. Bergeron & P. Boissé 1991; H.-W. Chen et al. 2010; N. M. Nielsen et al. 2013). This relation is typically modelled as a log-linear function:

$$\log W_{2796}\,(\text{Å}) = \alpha_1 b\,(\text{kpc}) + \beta_1 \tag{1}$$

where β_1 is the intercept at $b = 0$ and α_1 defines the exponential scale. For the redshift range $0 < z < 1.5$, we adopt $\alpha_1 = -0.019 \pm 0.002$ and $\beta_1 = 0.540 \pm 0.028$ from L. K. Guha, R. Srianand & P. Petitjean (2024). Since 82.63 per cent of the absorbers in our sample lie within this redshift interval, this is well suited for our analysis. The probability that one will detect Mg II absorption at a given b can be obtained from the measured covering factor (f_c) as a function of b. This can be modelled as:

$$f_c = A_{100}\left(\frac{b}{100\,\text{kpc}}\right)^{\gamma}, \tag{2}$$

Here A_{100} is given as:

$$A_{100} = A \times (1+z)^{\alpha_2}\left(\frac{M_*}{10^{10}\,\text{M}_\odot}\right)^{\beta_2}. \tag{3}$$

We adopt the best-fitting parameters γ and A_{100} from T.-W. Lan (2020), using their average values derived for star-forming galaxies. The normalization A_{100} corresponds to typical L^* galaxies

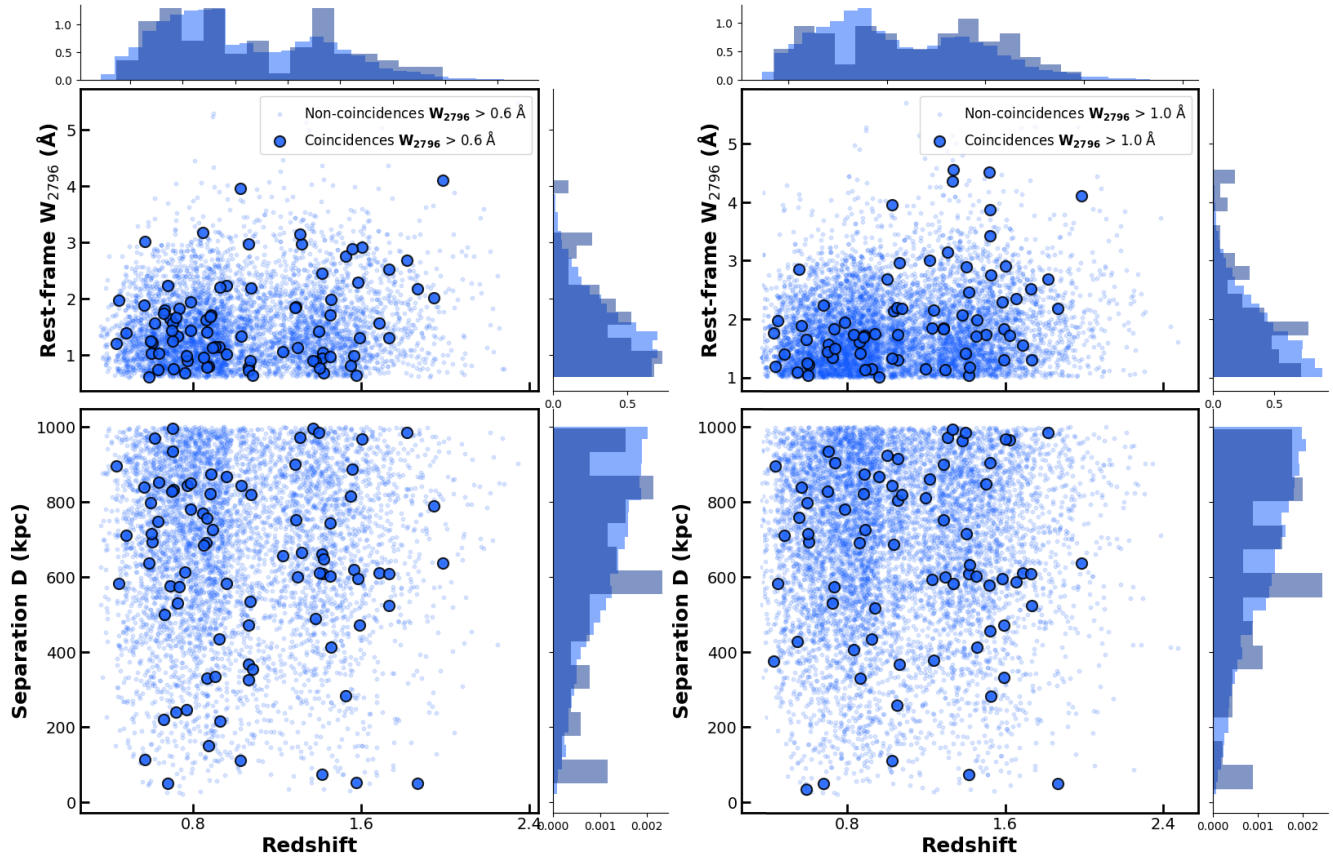

Figure 1. Distribution of pairs for two equivalent width thresholds ($W_{2796} > 0.6$ Å and $W_{2796} > 1.0$ Å). Top panels show the rest-frame equivalent width of detected absorbers, W_{2796}, as a function of absorber redshift, while bottom panels display the projected separation between the quasar sightlines, D, as a function of absorber redshift. The equivalent width shown corresponds to the absorber detected along the reference sightline used to initiate the coincidence search in the companion spectrum. Coincident absorbers are highlighted with larger, outlined symbols, whereas non-coincident systems are shown with smaller, fainter points. The marginal histograms along the top and right of each panel show the normalized distributions of absorber redshift and equivalent width (top panels) or projected separation (bottom panels), respectively, allowing a direct visual comparison between the coincident and non-coincident samples independent of sample size.

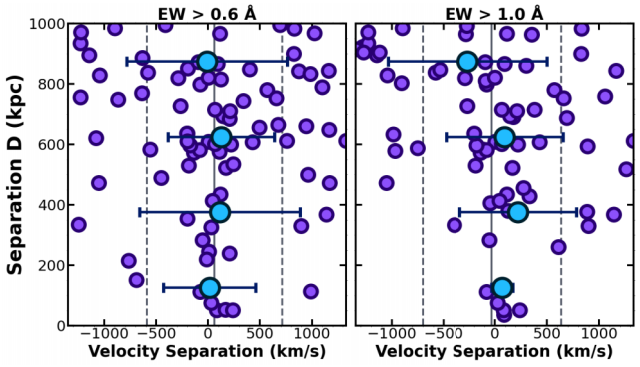

Figure 2. Scatter plots of line-of-sight velocity separation as a function of projected separation for coincident Mg II absorbers. The two panels show results for equivalent-width sensitivity thresholds of $W_{2796} > 0.6$ Å (left) and $W_{2796} > 1.0$ Å (right). Individual points represent measured velocity offsets for coincident systems, while the overplotted symbols with horizontal error bars indicate the mean velocity separation in bins (250 kpc) of projected separation D, with the error bars denoting the corresponding dispersion within each bin. The solid vertical line marks the mean velocity separation of the full sample, while the dashed lines indicate the $\pm 1\sigma$ dispersion from a Gaussian fit to the velocity distribution.

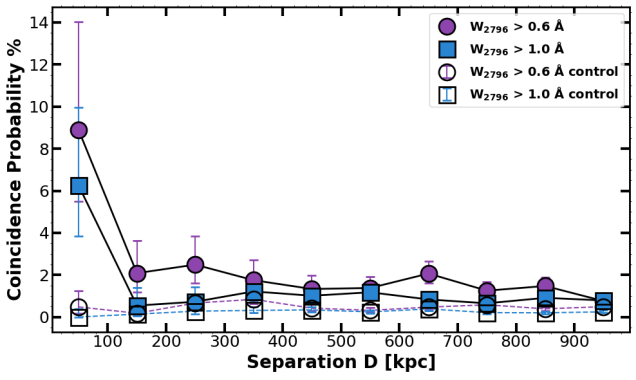

Figure 3. Coincidence probability (per cent) as a function of projected pair separation D at the absorber redshift. It is shown for two equivalent-width thresholds, $W_{2796} > 0.6$ Å (circles) and $W_{2796} > 1.0$ Å (squares). The corresponding control samples, are shown with unfilled symbols. Error bars represent binomial uncertainties corresponding to a 68 per cent (1σ) confidence interval.

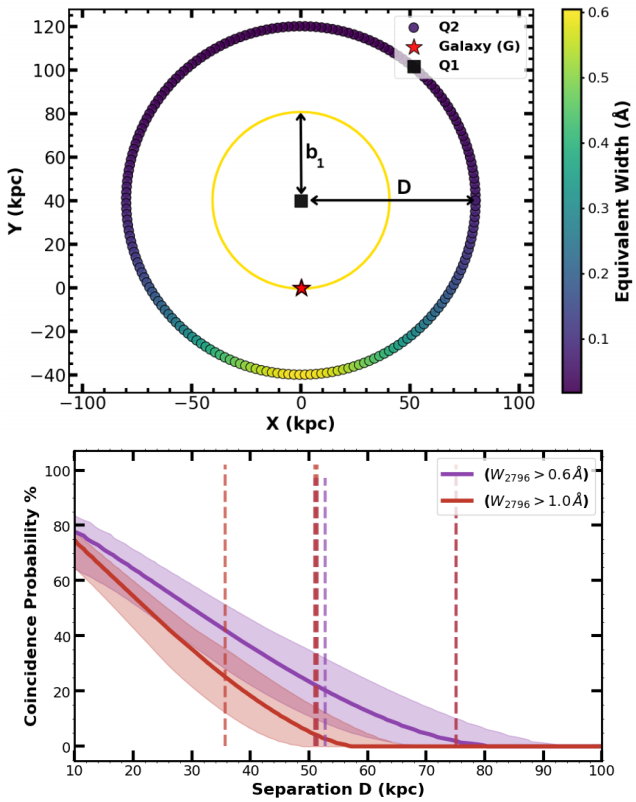

Figure 4. Top panel: illustrating an example of modelling coincidence probability using a single halo. Suppose the Q1 sightline shows a Mg II 2796 absorption with $W_{2796} = 0.6$ Å. Using the W–D relation, we infer the galaxy lies at an impact parameter of 40.10 kpc. The plot then shows all possible Q2 positions at projected separation (60 kpc) from the quasar Q1, and the corresponding W_{2796} values computed using the same relation. Bottom panel: variation of the coincidence probability, $P_{\rm coinc}$, with the projected separation between Q1 and Q2 at the absorber redshift. The vertical lines indicate the projected separations of the observed absorbers at which the coincidence–probability curve was sampled.

with a stellar mass of $M = 10^{10.8}\,{\rm M}_{\odot}$ at redshift $z = 1$, consistent with the median absorber redshift in our sample.

Let Q1 and Q2 are the two quasars which are separated by a small projected separation (D) in the sky. For an Mg II absorber of rest-equivalent width W_{2796} detected in the spectrum of Q1, the W–b relation (equation 1) implies a corresponding galaxy at an impact parameter b_1. The galaxy may therefore lie anywhere along a circle of radius b_1 centred on Q1, as illustrated in the top panel of Fig. 4. For a quasar pair with projected separation D, each possible galaxy position generates a different galaxy–Q2 impact parameter (b_2). This is geometrically equivalent to fixing the galaxy at one location and allowing Q2 to move along a circle of radius D around Q1. Applying the W–b relation to each such configuration yields a predicted equivalent width along Q2. The coincidence probability at separation D is then given by the fraction of the circle for which the predicted width exceeds the adopted threshold, multiplied by the covering fraction (equation 2).

To incorporate the distribution of observed absorber strengths, we repeat this procedure over a range of initial equivalent widths W_1 detected in Q1. For the $W_{2796} > 0.6$ Å and $W_{2796} > 1.0$ Å samples, we sample W_1 uniformly using 20 equally spaced values over the ranges 0.6–3.0 Å and 1.0–3.0 Å, respectively. Each W_1 maps to an impact parameter b_1 via equation (1), producing a set of coincidence probabilities for each D. The final coincidence probability curve is obtained by taking the weighted mean of these individual curves, using the exponential equivalent width distribution

$$p(W_{2796}) = \frac{1}{W_*} \exp\left(-\frac{W_{2796}}{W_*}\right), \quad (4)$$

as the weighting function, with $W_* = 0.702 \pm 0.017$ Å characterizing the observed distribution of Mg II absorber strengths (see D. B. Nestor, D. A. Turnshek & S. M. Rao 2005). This weighted mean represents the expected probability of detecting coincident absorption as a function of projected separation (D) and detection threshold. Uncertainties are propagated by varying all model parameters within their 1σ bounds. The resulting upper and lower bounds define the shaded uncertainty region in the bottom panel of Fig. 4.

If we sample the modelled coincidence probability curves at the observed projected quasar separations, the mean probabilities for the $W_{2796} > 0.6$ Å and $W_{2796} > 1.0$ Å thresholds are $0.149^{+0.112}_{-0.087}$ and $0.069^{+0.083}_{-0.045}$, respectively. The corresponding observed coincidence probabilities are $0.088^{+0.051}_{-0.033}$ and $0.062^{+0.037}_{-0.023}$, respectively which agree to the modelled probabilities within 1σ level. To investigate whether the coincidence probability evolves with redshift, we repeated the analysis at two additional redshifts corresponding to the lower 25th and higher 75th percentiles of our sample, located at $z = 0.73$ and $z = 1.35$, respectively. At $z = 0.7278$, the predicted mean coincidence probabilities are $0.133^{+0.105}_{-0.077}$ for the $W_{2796} > 0.6$ Å threshold and $0.056^{+0.072}_{-0.037}$ for the $W_{2796} > 1.0$ Å threshold. At the redshift of $z = 1.3688$, these values increase to $0.166^{+0.108}_{-0.096}$ and $0.084^{+0.075}_{-0.053}$, respectively. These results reveal a mild but systematic increase in coincidence probability with redshift, and since the covering fraction itself is known to increase with redshift, this naturally drives the observed rise in coincidence probability.

3.2 Modelling the coincident probability due to clustering

While the single-halo model naturally explains the rapid rise in coincidence probability at separations below ∼100 kpc, the observed plateau at larger separations must arise from a different physical mechanism. On scales of several hundred kiloparsecs to a few megaparsecs, Mg II absorbers are expected to correlate with the surrounding galaxy population through large-scale structure (N. Bouché, M. T. Murphy & C. Péroux 2004; J.-R. Gauthier, H.-W. Chen & J. L. Tinker 2009; B. F. Lundgren et al. 2009). To estimate the coincidence probability due to galaxy clustering, we use pairs as reference sightlines. First, we address this problem using available photometric redshift catalogue of galaxies.

For each pair, the quasar's position and absorber redshift define a cylindrical search volume of radius 1000 kpc and line-of-sight depth corresponding to a velocity range of ±1500 km s^{-1}, converted to a redshift interval around the absorber redshift (see the schematic illustration in the top panel of Fig. 5). In constructing these cylinders, we use the RA, Dec, and absorber redshift ($z_{\rm abs}$) from our quasar sample and restrict the analysis to systems with $0.4 < z_{\rm abs} < 0.7$, corresponding to the redshift range where the photometric galaxy catalogue from the DESI Legacy Imaging Surveys DR10 remains well characterized in terms of depth and completeness (A. Dey et al. 2019). The survey provides wide-area optical imaging reaching typical 5σ point-source depths of $g \simeq$

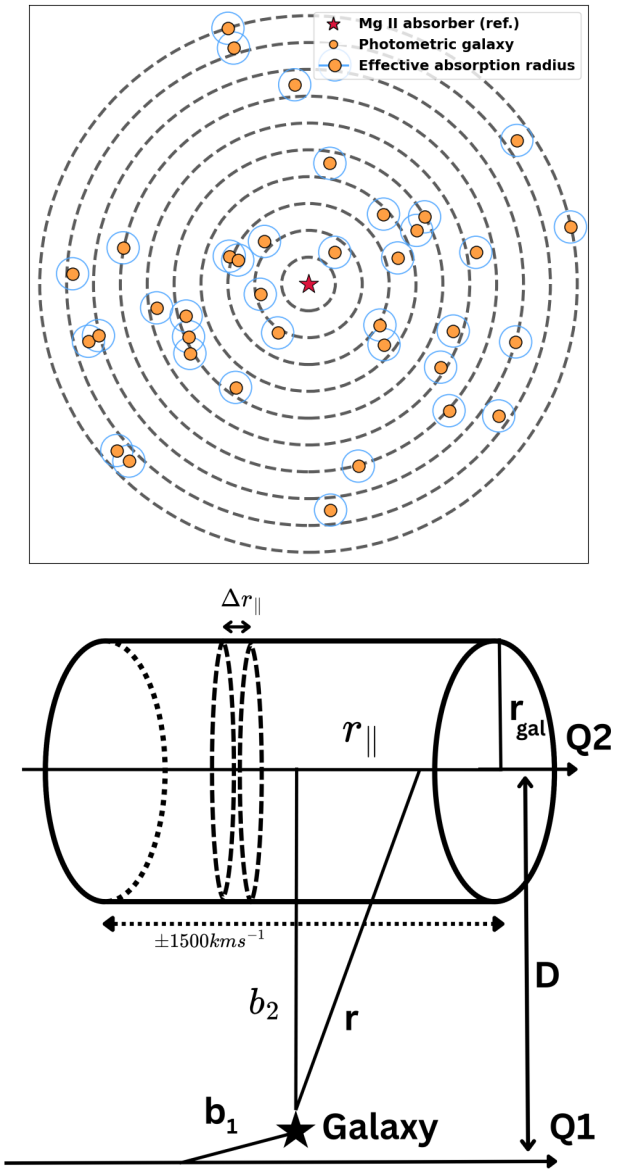

Figure 5. Top panel: Schematic illustration of the projected-shell method used to estimate the coincidence probability arising from galaxy clustering. Concentric annuli (100 kpc width) are drawn around each reference Mg II absorber. Photometric galaxies from the Legacy Survey DR10 within the redshift interval $0.4 < z_{abs} < 0.7$ are shown with their corresponding effective absorption radii (40 and 20 kpc for equivalent-width thresholds of 0.6 and 1.0 Å, respectively). Only absorbers within this redshift range and within the DR10 footprint are used in the analysis. Bottom panel: schematic illustration of the clustering-based model used to estimate the theoretical coincidence probability. Given an Mg II detection in the first sightline (Q1) at impact parameter b_1, a cylindrical volume is constructed around the second sightline (Q2) with radius $r_{gal}(W_{2796})$ and a line-of-sight half-length corresponding to ± 1500 km s^{-1}. The expected number of galaxies within this cylinder is computed by integrating the galaxy two-point correlation function $\xi(r) = (r/r_0)^{-\gamma}$, and is interpreted as the probability of detecting a coincident absorber as a function of the projected separation D.

24.0, $r \simeq 23.4$, and $z \simeq 22.5$ AB magnitudes for faint galaxies. We then count photometric galaxies that fall within these cylindrical volumes. Since photometric redshifts carry significant uncertainties, typically σ_{NMAD} (Normalized Median Absolute Deviation) ~ 0.01–0.02 when compared with spectroscopic redshifts (C. Li et al. 2024), each galaxy is treated as a Gaussian in redshift space, with its mean given by the photometric redshift and standard deviation equal to its reported photo-z error. For each absorber, we compute the probability that a given photometric galaxy lies within the absorber's redshift range by integrating this Gaussian across the corresponding Δz interval (± 1500 kms^{-1}). The contribution of each galaxy to the total probability is thus weighted by this overlap fraction.

To quantify the radial dependence within 1000 kpc, we divide the projected separation into concentric cylindrical shells of thickness 100 kpc. Within each shell, we compute the probability-weighted volume fraction occupied by galaxies using

$$p_{\mathrm{sum,vol}} = \sum_i P_i \, (\pi \, r_{\mathrm{gal}}^2 \, h), \tag{5}$$

where P_i is the overlap probability for the ith galaxy, r_{gal} is the physical radius associated with the equivalent-width threshold (28.42 kpc for EW > 1 Å and 40.10 kpc for EW > 0.6 Å, derived from the observed W–b relation from equation 1), and h is the line-of-sight height of the absorber cylinder. This weighted volume is then normalized by the total shell volume,

$$V_{\mathrm{shell}} = \pi \, h \, (D_{\mathrm{outer}}^2 - D_{\mathrm{inner}}^2), \tag{6}$$

yielding the fractional volume within the shell expected to be occupied by galaxies capable of producing absorption. Finally, multiplying this fractional volume by the average covering fraction for the corresponding equivalent-width limit gives the probability of detecting an absorber along a background sightline – that is, the coincidence probability due to galaxy clustering. The resulting coincidence probability profile (Fig. 6) is approximately constant with projected separation, consistent with expectations for galaxy clustering on scales below $\sim$1 Mpc. However, the predicted probabilities are systematically lower by roughly a factor of two compared to the observed coincidence fractions for both equivalent-width thresholds. This discrepancy likely reflects two limitations of the methodology.

First, the Legacy Survey photometric catalogue is limited to relatively luminous galaxies. Z. Wang et al. (2021) constructed a volume-limited galaxy samples from the DESI Legacy Imaging Surveys (DR8) and report absolute magnitudes in the AB system, showing that at intermediate redshifts ($0.4 \lesssim z \lesssim 0.7$) the samples are complete only down to $M_z^{0.5} - 5 \log h \simeq -21$. For $h = 0.7$, this corresponds to $M_z^{0.5} \simeq -21.77$. The superscript '0.5' denotes that the magnitudes are k-corrected to a reference redshift $z = 0.5$. At this redshift, the observed z band ($\lambda_{\mathrm{eff}} \approx 9100$ Å) samples rest-frame optical wavelengths ($\lambda_{\mathrm{rest}} \approx 6000$ Å), close to the Johnson V band. We therefore interpret $M_z^{0.5}$ as tracing rest-frame V-band luminosity to first order, and convert to the B band using a typical rest-frame colour $(B - V) \simeq 0.6$ for typical galaxies (e.g. M. Fukugita, K. Shimasaku & T. Ichikawa 1995). Finally, we transform from the AB to the Vega system using the empirical calibration $B_{\mathrm{Vega}} = B_{\mathrm{AB}} + 0.163$ (Z. Frei et al. 1996). This corresponds to an approximate rest-frame Johnson B-band magnitude of $M_B^{\mathrm{Vega}} \simeq -21$. As a result, the Legacy Survey catalogue systematically misses fainter galaxies, which are known to contribute significantly to the population of Mg II absorber hosts. Second, our treatment of photometric redshifts approximating

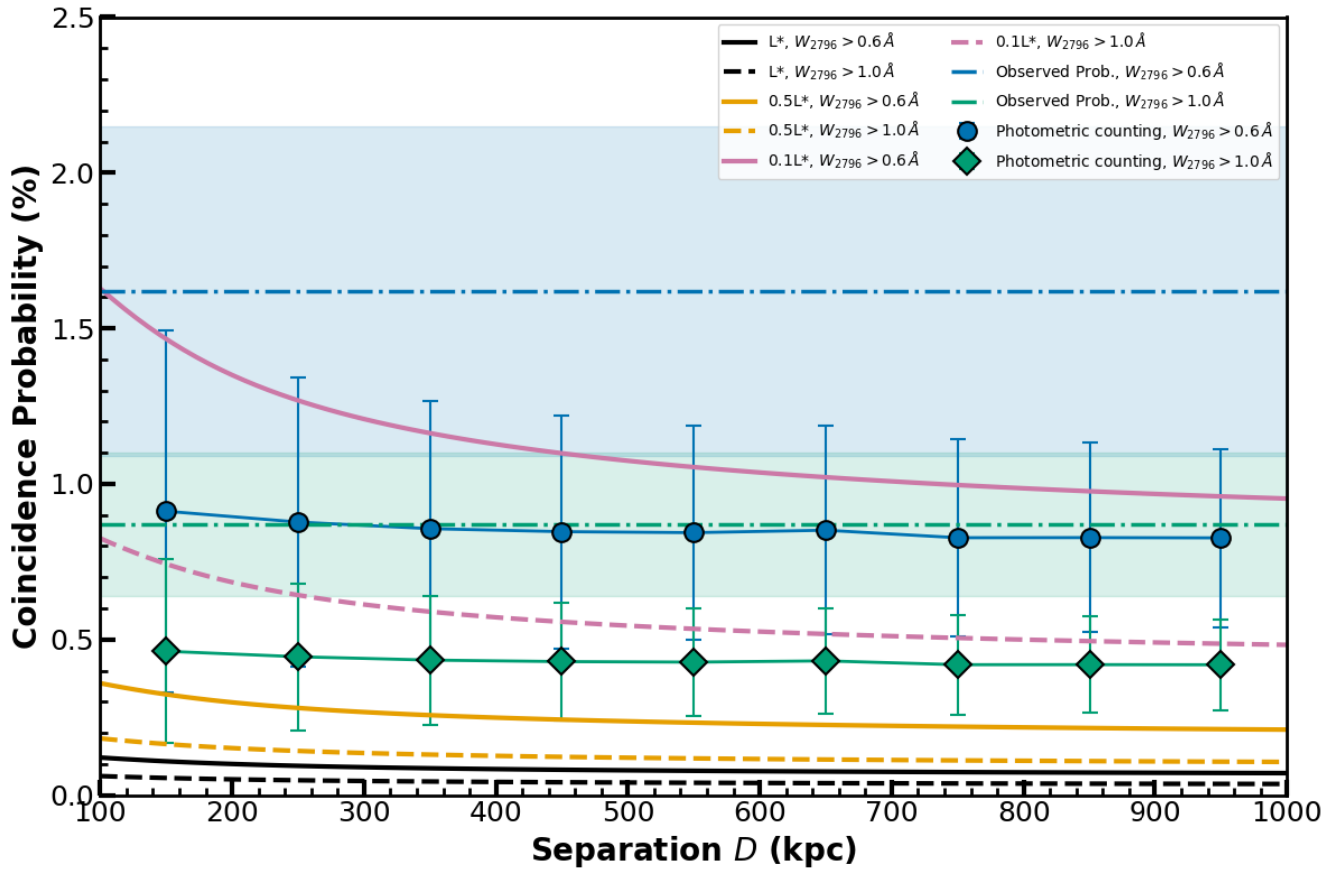

Figure 6. Coincidence probability due to clustering of Mg II absorbers as a function of projected separation D between quasar sightlines. The horizontal dot-dashed lines and shaded regions indicate the average observed coincidence probabilities and their 1σ uncertainties for absorbers with $W_{2796} > 0.6$ Å and $W_{2796} > 1.0$ Å, respectively. Points with error bars show the coincidence probability measured in radial bins from photometric galaxy counting for the same equivalent-width thresholds, corrected for the mean covering fraction. Solid and dashed curves represent theoretical predictions from the clustering model for $W_{2796} > 0.6$ Å and $W_{2796} > 1.0$ Å, respectively. For each equivalent-width threshold, the black, orange, and magenta curves correspond to models assuming characteristic host galaxy luminosities of L^*, $0.5L^*$, and $0.1L^*$, respectively, where the expected number of galaxies is computed by integrating the galaxy two-point correlation function within the cylindrical search volume.

each galaxy as a Gaussian in redshift space and integrating only the overlap with the absorber redshift window provides a conservative estimate of association probability and may down weight truly correlated galaxies. Hence this model should be regarded as a lower bound on the large-scale contribution, with the observed coincidence probabilities implying either a higher abundance of faint galaxy halos or broader redshift correlation than captured by our strict Gaussian weighting.

While the photometric-galaxy approach provides a fully empirical estimate of the clustering contribution, it is limited by photometric-redshift uncertainties and the finite depth of the imaging data. To verify that the inferred coincidence probabilities are not driven by these observational systematics, we complement this analysis with an independent theoretical estimate based on the galaxy two-point correlation function. Consider a quasar sightline (Q1) with a detected Mg II absorption system. Using W_{2796}–b relation from equation (1), the projected impact parameter between the absorber host galaxy and the Q1 sightline is inferred to be b_1. We then construct a cylindrical volume centred on the absorber, with a radius $r_{\rm gal}$ and a line-of-sight extent corresponding to a velocity interval of ± 1500 km s^{-1}. The radius $r_{\rm gal}$ taken from equation (1), represents the radius associated with the adopted equivalent-width threshold, taking values of $r_{\rm gal} = 28.42$ kpc for EW > 1 Å and $r_{\rm gal} = 40.10$ kpc for EW > 0.6 Å. A schematic diagram of this is shown in Fig. 5 bottom panel. The clustering-induced coincidence probability is then defined as the expected number of galaxies within this cylinder and is given by:

$$P_{\rm c} = \sum_{i=0}^{N} \pi r_{\rm gal}^2 \, n_0 \left[1 + \xi(r_i)\right] \Delta r_{\perp}, \tag{7}$$

where r is $b_2^2 + r_{\parallel}^2$, $\Delta r_{\parallel}$ the path-length element associated with the ith bin, n_o is the average galaxy number density and $\xi(r)$ is the two point correlation function which is defined as:

$$\xi(r) = \left(\frac{r}{r_0}\right)^{-\gamma}, \tag{8}$$

where r is the distance of the point in space from the galaxy, r_0 is the comoving correlation length, and γ is the slope of the correlation function. We adopt the clustering parameters r_0 and γ from measurements of galaxy clustering at $z \sim 1$ reported by A. L. Coil et al. (2004), based on the DEEP2 Galaxy Redshift Survey. The DEEP2 sample is R-band selected with a limiting magnitude of $R_{\rm AB} < 24.1$, corresponding approximately to an absolute magnitude limit of $M_B \sim -20$ to -20.5 at $z \sim 1$, depending on

galaxy spectral type. The adopted values of r_0 and γ therefore characterize the clustering of galaxies with luminosities near L^* at these redshifts. To calculate the galaxy number density relevant for Mg II absorption, we derive n_0 from the rest-frame B-band Schechter luminosity function measured by S. M. Faber et al. (2007). We adopt the parameters corresponding to the $z \simeq 1$ bin, with $\phi_* = 3.304 \times 10^{-3}$ Mpc^{-3}, $M_* = -21.36$, and a fixed faint-end slope $\alpha = -1.30$, and propagate the quoted uncertainties in ϕ_* and M_*. The Schechter function is integrated down to luminosity thresholds corresponding to three characteristic galaxy populations, namely L^*, $0.5L^*$, and $0.1L^*$, yielding comoving number densities appropriate for each luminosity bin. These densities are subsequently converted to proper units at $z = 1$ using

$$n_{\rm proper} = n_{\rm comoving}(1+z)^3. \tag{9}$$

The resulting clustering-based coincidence probabilities as a function of projected separation are shown in Fig. 6. Among the three luminosity thresholds considered, the model assuming a characteristic luminosity of $0.1L^*$ provides the best overall agreement with the observed coincidence probability as a function of separation. The models based on brighter galaxy populations (L^* and $0.5L^*$) systematically under predict the observed signal at most separations. We note that the coincidence probabilities inferred from photometric galaxy counting are consistently lower than the clustering-based predictions, which may reflect residual incompleteness in the photometric sample or uncertainties in the adopted covering fraction correction. It is well established that the comoving correlation length evolves with redshift as a consequence of the growth of large-scale structure and the changing bias of the galaxy population. In general, clustering measurements show weaker intrinsic matter clustering at higher redshift, while the observed galaxy clustering reflects the combined effects of structure growth and galaxy bias (e.g. A. L. Coil et al. 2004; I. Zehavi et al. 2011; Z. Wang et al. 2021), such that typical values of r_0 at $z \sim 1$ are smaller than those measured in the local Universe. A smaller correlation length reduces the amplitude of the two-point correlation function, $\xi(r)$, thereby lowering the expected excess number of galaxies within the cylindrical search volume. At the same time, when expressed in proper units, the galaxy number density increases with redshift according to $n_{\rm proper} = n_{\rm comoving}(1+z)^3$, which partially compensates for the reduced clustering amplitude. In this work, we compute the clustering-based coincidence probability at $z \simeq 1$, corresponding to the median redshift of the Mg II absorber sample, ensuring that the adopted clustering parameters and number densities are appropriate for the redshift range probed by our data.

3.3 Stacking

Next, we investigate coincident Mg II absorption using stacking method. For this, we stack the spectrum of the second sightline for systems in which the first sightline contains a detected Mg II absorber. Two sub-samples from the sample of 25 764 pairs (see Table 1 line 3) are defined based on the rest-frame equivalent width measured in the first sightline, with thresholds of $W_{2796} > 0.6$ Å (22557 pairs) and $W_{2796} > 1.0$ Å (16684 pairs). In addition, we perform the stacking analysis on the full sample without imposing any equivalent-width threshold in the first sightline. For each system, the normalized spectrum of the opposite sightline is shifted to the absorber rest frame using the corresponding absorption redshift, and a ± 50 Å window centred on the Mg II doublet is extracted. The continuum is again normalized by dividing by the median flux within this window. To estimate the noise level for each individual spectrum, we compute the root-mean-square (RMS) scatter of the flux residuals within this window, applying a 3σ clipping to remove outliers. All spectra are interpolated onto a common rest-frame wavelength grid spanning 2750–2850 Å. The spectra are then grouped into projected separation (D) bins of width 200 kpc and combined using an inverse–variance weighted mean, where the weights of pixels are defined by the inverse square of RMS noise of individual spectrum. This procedure yields a stacked flux profile for each separation bin. The statistical uncertainty on the stacked spectrum is estimated from the inverse square root of the summed weights, while an empirical error spectrum is also computed from the RMS scatter among the contributing spectra divided by the effective number of sightlines contributing to each wavelength bin.

Each stacked spectrum is fitted with a two component Gaussian absorption model representing the Mg II λλ2796, 2803 doublet, allowing for a common velocity width and a small global wavelength shift. The rest-frame equivalent widths are measured by integrating the absorption flux profile within $\pm 3\sigma$ of the fitted line centres. This procedure yields the stacked Mg II absorption strength in the second sightline as a function of projected separation (Fig. 7). For projected separations $D < 200$ kpc, we measure a stacked equivalent width of $W_{2796} = 0.0866 \pm 0.0116$ Å for the full sample, $W_{2796} = 0.0942 \pm 0.0148$ Å for the threshold $W_{2796} > 1.0$ Å subsample, and $W_{2796} = 0.0862 \pm 0.0126$ Å for the threshold $W_{2796} > 0.6$ Å subsample. We find that the stacked equivalent width declines rapidly with increasing projected separation and becomes comparable to the amplitude of residual continuum fluctuations beyond $D \gtrsim 200$ kpc. Visual inspection of the stacked spectra in these bins shows no statistically significant Mg II doublet relative to the local spectral fluctuations arising from noise and imperfect continuum normalization. We therefore treat measurements at $D > 200$ kpc as non-detections and present them as upper limits in our analysis.

As an additional check, we perform an identical stacking analysis on a control sample in which the same fitting procedure is applied to wavelength regions offset by 25 Å from the Mg II doublet. The resulting equivalent widths are consistent with zero at all separations, confirming that the weak signals observed at small projected separations are not produced by systematic effects in the stacking or fitting procedure. We further repeat the stacking analysis by dividing the full sample into two redshift subsamples at the median absorber redshift, $z = 1$. For projected separations $D < 200$ kpc, we measure a stacked equivalent width of $W_{2796} = 0.1151 \pm 0.0182$ Å for the high-redshift subsample ($z \geq 1$), compared to $W_{2796} = 0.0616 \pm 0.0142$ Å for the low-redshift subsample ($z < 1$). This indicates an increase in the stacked Mg II absorption strength with redshift at small projected separations.

We model the stacked equivalent width at a given projected separation D is as:

$$\langle W_{\rm stack}(D) \rangle = P(D) \int_{W_{\rm min}}^{W_{\rm max}} W\, p(W)\, {\rm d}W, \tag{10}$$

where $P(D)$ is the coincidence probability measured observationally (Fig. 3), and $p(W)$ is probability per unit equivalent width as defined in equation (4). The $W_{\rm min}$ and $W_{\rm max}$ range corresponds to 0.6–4 Å and 1–4 Å for threshold $W_{2796} > 0.6$ Å and $W_{2796} > 1$ Å sample respectively. Here, the dependence on projected separation enters entirely through the observed coincidence probability.

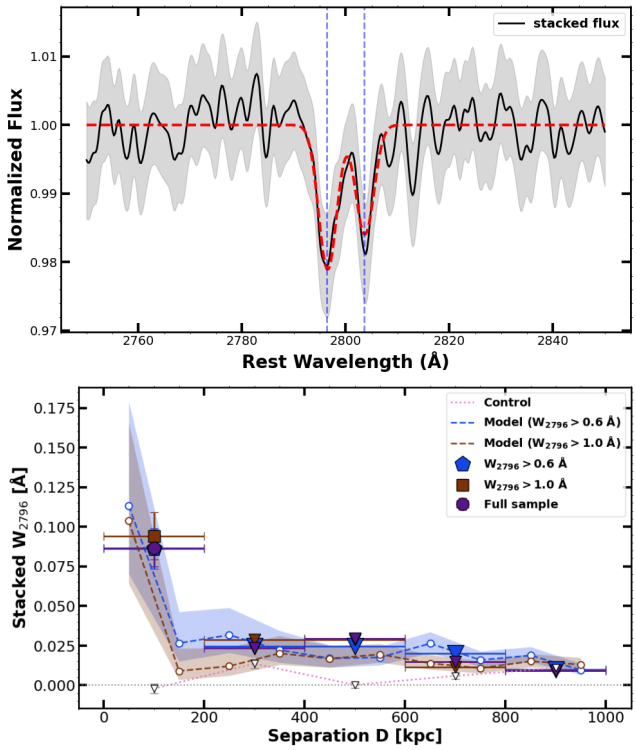

Figure 7. Top panel: example stacked spectrum in the Mg II λλ2796, 2803 region for pairs with projected separations $D = 0$–200 kpc. Bottom panel: stacked Mg II λ2796 equivalent width measured in the second sightline of pairs as a function of projected separation. Symbols show the observed stacked equivalent widths for systems in which the first sightline contains an absorber with $W_{2796} > 0.6$ Å (diamond) and $W_{2796} > 1.0$ Å (square), while circles correspond to the full sample. Measurements at $D \leq 200$ kpc represent statistically significant detections, whereas points at larger separations are shown as upper limits. Horizontal error bars indicate the projected-separation bin width (200 kpc) used in the stacking analysis. The dotted curve shows the result from a control sample constructed by stacking offset wavelength regions. Dashed curves show the corresponding model predictions derived from the observed coincidence probabilities (e.g. see equation 10).

Using the empirically measured $P(D)$ for the two equivalent-width thresholds ($W_{2796} > 0.6$ Å and $W_{2796} > 1.0$ Å), we compute model predictions for the stacked Mg II absorption as a function of projected separation. The resulting model predictions are shown in Fig. 7 and are compared directly with the measured stacked Mg II equivalent widths. For projected separations $D \lesssim 200$ kpc, the model predicts a stacked equivalent width of $\langle W_{\rm stack} \rangle = 0.096^{+0.056}_{-0.036}$ Å for the $W_{2796} > 0.6$ Å threshold and $\langle W_{\rm stack} \rangle = 0.091^{+0.054}_{-0.034}$ Å for the $W_{2796} > 1.0$ Å threshold, in excellent agreement with the observed stacked measurements. The model successfully reproduces both the amplitude and the separation dependence of the stacked absorption signal, with the enhanced equivalent width at small separations arising naturally from the elevated coincidence probability in this regime. At larger separations, the flattening of the stacked equivalent width reflects the corresponding decline and plateau in $P(D)$. This close agreement indicates that the observed stacked Mg II absorption is primarily governed by the probability of intersecting an absorber at a given projected separation.

4 DISCUSSION AND CONCLUSIONS

The coincidence probability curve derived from our pair sample exhibits a clear two-regime structure. At separations below ∼100 kpc, the coincidence probability rises sharply, reaching values of ∼5–8 per cent (see Fig. 3). This steep increase indicates that sightlines within $\lesssim$100 kpc have a significantly enhanced likelihood of intersecting the same Mg II-absorbing structure, consistent with both sightlines probing the same dark-matter halo or an extended region of correlated cool gas within the CGM. Beyond ∼100−200 kpc, the coincidence probability declines rapidly and settles into a low plateau of ∼1–2 per cent that persists out to nearly 1 Mpc.

To interpret these trends, we compared the observed curve to simple physical models. A single-halo model naturally reproduces the strong enhancement below ∼100 kpc, indicating that the high coincidence probability in this regime originates from gas associated with a common halo and its extended CGM. At larger separations, where the coincidence probability remains non-zero but at the ∼1–2 per cent level, the single-halo model cannot account for the observed behaviour. We show that this low plateau is well explained by galaxy clustering: both direct photometric galaxy counts and the two-point correlation function predict a small but finite chance that two widely separated sightlines intersect independent Mg II absorbers hosted by galaxies correlated in large-scale structure. Thus, the full coincidence curve can be understood as the sum of a halo-driven component at small separations and a clustering-driven component at large separations.

Our measured coincidence probabilities are lower than those reported by D. Tytler et al. (2009), who found coincidence fractions of $\gtrsim$50 per cent at $D < 100$ kpc that decline to ∼ 0.8 per cent at $D \sim$ 1–2 Mpc. Despite this difference in normalization, the overall trend with transverse separation is qualitatively similar in both studies, with the coincidence probability decreasing rapidly with increasing separation and approaching very small values on Mpc scales. The higher coincidence fractions reported by D. Tytler et al. (2009) likely arise from differences in sample selection and methodology, as their analysis focused primarily on higher-redshift ($z \sim 2$) absorbers and included multiple metal species, particularly C IV, which traces a more extended and highly ionized gas phase. In addition, their coincidence definition allowed matches between different ions (e.g. C IV–Mg II), whereas our analysis requires a strict Mg II–Mg II coincidence with uniform equivalent-width thresholds.

A recent study by H. Cortés-Muñoz et al. (2026) analysed the clustering of C IV absorbers using high-resolution spectra of quasar pairs and lensed quasars spanning transverse separations from sub-kiloparsec to megaparsec scales. They reported evidence for multiple coherence scales in the C IV correlation function, with a small-scale break at $r_2 \approx 4.7^{+1.6}_{-1.2}$ kpc interpreted as the characteristic size of individual C IV-bearing clouds, and a larger-scale break at $r_1 \approx 654$ kpc associated with the extent of enriched regions around galaxies. Between these scales the correlation function flattens, while it declines again at larger separations. In contrast, our Mg II coincidence probabilities remain approximately constant at large separations ($\gtrsim$200 kpc), consistent with expectations from galaxy clustering. Part of this difference arises from the range of scales probed by the two studies. The small-scale break reported for C IV occurs at a few kiloparsecs, which is below the minimum transverse separation accessible in our quasar-pair sample and therefore cannot be directly tested here.

The larger-scale break in the C IV correlation function occurs near ∼650 kpc, reflecting the more extended distribution of highly ionized gas. In our Mg II measurements the transition occurs at smaller scales (∼100–200 kpc), marking the point where coincidences transition from being dominated by gas within a common halo to those produced by galaxy clustering. This difference is likely related to the distinct physical phases traced by the two ions. C IV traces a warmer and more highly ionized gas phase that is expected to extend farther into the CGM and surrounding intergalactic environment, whereas Mg II predominantly traces denser, cooler gas confined to inner halo regions. As a result, C IV correlations may remain sensitive to the structure of enriched regions on larger scales, while Mg II coincidences at similar separations are dominated primarily by the clustering of host galaxies rather than by coherent gas structures.

Our single-halo model predicts a high coincidence probability, reaching ∼80 per cent at separations $D \lesssim 20$ kpc, reflecting the expected coherence of Mg II-absorbing gas within the inner CGM. Although our quasar-pair sample does not probe such small separations, independent studies of strongly lensed quasars provide important constraints on the spatial structure of Mg II-bearing gas on kiloparsec scales. Observations of multi-image gravitational lenses frequently detect Mg II absorption along multiple closely spaced sightlines, indicating a high covering fraction and substantial coherence at small separations (e.g. H.-W. Chen et al. 2014; F. S. Zahedy et al. 2016; R. Augustin et al. 2021; K. Okoshi et al. 2021). However, these absorbers also exhibit significant sightline-to-sightline variations. For example, J. A. Rogerson & P. B. Hall (2012) showed that the observed scatter in Mg II equivalent widths requires a small coherence length ($\ell_c \simeq 0.5\,h^{-1}$ kpc), while other studies report variations of $\lesssim$40 per cent across separations of ∼8–22 kpc (K. H. R. Rubin et al. 2018). Complementary constraints from gravitational-arc spectroscopy further support this picture, revealing Mg II absorption across many closely spaced sightlines and implying coherence on kiloparsec scales (S. Lopez et al. 2018; A. Afruni et al. 2023; A. Shaban et al. 2025). These observational constraints are broadly consistent with recent theoretical expectations for the structure of the cool CGM. High-resolution cosmological simulations such as TNG50 predict that the Mg II-bearing CGM is composed of numerous compact cloudlets with characteristic sizes of order ∼kpc or smaller (D. Nelson et al. 2020), while zoom-in simulations likewise show that Mg II absorption can arise from dense small-scale structures embedded within halo gas (R. Ramesh & D. Nelson 2024). Spectral modelling studies also infer a fragmented multiphase CGM in which multiple discrete clouds contribute to the absorption along a single sightline (Sameer et al. 2024). Taken together, these observations suggest that Mg II absorption arises from numerous small-scale structures within galaxy halos, producing a combination of high covering fraction and significant small-scale variability. This picture is broadly consistent with the high coincidence probabilities predicted by our single-halo model at small impact parameters.

It is important to note, however, that our single-halo model is constructed using the observed W–D relation and therefore describes the average radial behaviour of Mg II absorption, implicitly assuming a smooth distribution of absorbing gas at fixed impact parameter. As such, the model does not explicitly incorporate small-scale spatial inhomogeneities or a clumpy cloudlet structure in the CGM. The strong sightline-to-sightline variations observed in lensed quasar systems instead suggest that Mg II-bearing gas is highly fragmented on kiloparsec and sub-kiloparsec scales. In this context, the high coincidence probabilities predicted by our model at small separations should be interpreted as reflecting the ensemble-averaged covering fraction of such cloudlets, rather than a spatially coherent medium.

Our stacking analysis provides independent support for this picture. For sightlines lacking individual Mg II detections, stacked spectra show a significant excess in mean equivalent width on the side where the paired sightline does not exhibits absorption. This enhancement extends to separations of ∼100–200 kpc, suggesting that Mg II absorption is correlated across these scales even when the individual features fall below the detection threshold. The stacking therefore constrains the characteristic length of the Mg II-bearing CGM to be of order ∼100–200 kpc, consistent with the interpretation of the coincidence curve. Using the observed coincidence probability, we show that the measured stacked equivalent widths are naturally reproduced by a simple physically motivated model. Our stacked measurements at small projected separations are broadly consistent with independent DESI-based stacking analyses of Mg II absorption around galaxies at comparable redshifts (Z. Chen et al. 2025). Restricting our sample to projected separations $D < 200$ kpc, the median separation is $D_{\rm med} \simeq 140$ kpc, at which we measure a stacked equivalent width of $W_{2796} \sim 0.1$ Å. At comparable projected separations (∼140 kpc), the DESI-based stacking analysis of Z. Chen et al. (2025) reports similar Mg II equivalent widths of order $W_{2796} \sim 0.1$ Å for galaxies at $z \sim 1$. This agreement indicates that, despite differences in sample selection and methodology, both studies recover a consistent amplitude and radial decline of Mg II absorption within the inner ∼200 kpc of the CGM.

Together, these results indicate that Mg II absorption exhibits strong sightline correlations within the inner ∼100 kpc of galaxy halos, while at larger separations the correlations are dominated by galaxy clustering rather than by gas confined to a single halo. Our measurements therefore identify the transition scale between the halo regime and the large-scale-structure regime, bridging the gap between sub-kpc coherence constraints from lensed quasars and Mpc-scale absorber clustering studies. Future work will require substantially larger samples of quasar pairs at smaller transverse separations in order to more densely sample the rising portion of the coincidence and stacking curves. Such observations will enable a more precise characterization of the spatial coherence, characteristic scales, and internal structure of the Mg II-bearing cool CGM in the inner halo regime.

ACKNOWLEDGEMENTS

The research of PS is supported by the University Grants Commission (UGC), Government of India, under the UGC-JRF scheme (Ref. No.: 221610014755). HC and PS express their gratitude to the Inter-University Centre for Astronomy and Astrophysics (IUCAA) for their hospitality and the provision of High-Performance Computing (HPC) facilities under the IUCAA Associate Programme. Additionally, we acknowledge the assistance of AI tools, specifically OpenAI's CHATGPT, for aiding in writing and code development, and GRAMMARLY for enhancing the text's clarity and correctness.

DATA AVAILABILITY

The data used in this study are publicly available in the SDSS DR16 Data Release.

REFERENCES

Afruni A. et al., 2023, A&A, 680, A112
Anand A., Nelson D., Kauffmann G., 2021, MNRAS, 504, 65
Augustin R., Péroux C., Hamanowicz A., Kulkarni V., Rahmani H., Zanella A., 2021, MNRAS, 505, 6195
Bergeron J., Boissé P., 1991, A&A, 243, 344
Bouché N., Murphy M. T., Péroux C., 2004, MNRAS, 354, L25
Burbidge E. M., 1967, ARA&A, 5, 399
Burbidge E. M., Lynds C. R., Burbidge G. R., 1966, ApJ, 144, 447
Chen H.-W., Helsby J. E., Gauthier J.-R., Shectman S. A., Thompson I. B., Tinker J. L., 2010, ApJ, 714, 1521
Chen H.-W., Gauthier J.-R., Sharon K., Johnson S. D., Nair P., Liang C. J., 2014, MNRAS, 438, 1435
Chen Z. et al., 2025, ApJ, 981, 81
Churchill C. W., 2025, preprint (arXiv:2510.23803)
Coil A. L. et al., 2004, ApJ, 609, 525
Cortés-Muñoz H. et al., 2026, A&A, 707, A178
Dey A. et al., 2019, AJ, 157, 168
Dutta R., Acebron A., Fumagalli M., Grillo C., Caminha G. B., Fossati M., 2024, MNRAS, 528, 1895
Ellison S. L., Ibata R., Pettini M., Lewis G. F., Aracil B., Petitjean P., Srianand R., 2004, A&A, 414, 79
Faber S. M. et al., 2007, ApJ, 665, 265
Frei Z., Guhathakurta P., Gunn J. E., Tyson J. A., 1996, AJ, 111, 174
Fukugita M., Shimasaku K., Ichikawa T., 1995, PASP, 107, 945
Fumagalli M., 2024, preprint (arXiv:2409.00174)
Gauthier J.-R., Chen H.-W., Tinker J. L., 2009, ApJ, 702, 50
Gontcho A Gontcho S., Miralda-Escudé J., Font-Ribera A., Blomqvist M., Busca N. G., Rich J., 2018, MNRAS, 480, 610
Guha L. K., Srianand R., Petitjean P., 2024, MNRAS, 527, 5075
Gunn J. E., Peterson B. A., 1965, ApJ, 142, 1633
Jalan P., Chand H., Srianand R., 2019, ApJ, 884, 151
Lan T.-W., 2020, ApJ, 897, 97
Li C. et al., 2024, AJ, 168, 233
Lopez S. et al., 2018, Nature, 554, 493
Lundgren B. F. et al., 2009, ApJ, 698, 819
Lyke B. W. et al., 2020, ApJS, 250, 8
Nelson D. et al., 2020, MNRAS, 498, 2391
Nestor D. B., Turnshek D. A., Rao S. M., 2005, ApJ, 628, 637
Nielsen N. M., Churchill C. W., Kacprzak G. G., Murphy M. T., 2013, ApJ, 776, 114
Okoshi K. et al., 2021, AJ, 162, 175
Ramesh R., Nelson D., 2024, MNRAS, 528, 3320
Rogerson J. A., Hall P. B., 2012, MNRAS, 421, 971
Rubin K. H. R., Hennawi J. F., Prochaska J. X., Simcoe R. A., Myers A., Lau M. W., 2015, ApJ, 808, 38
Rubin K. H. R. et al., 2018, ApJ, 859, 146
Sameer et al., 2024, MNRAS, 530, 3827
Sandage A., 1965, ApJ, 141, 1560
Shaban A. et al., 2025, ApJ, 986, 190
Sharma P., Srianand R., Chand H., Guha L. K., 2025, MNRAS, 541, 601
Srianand R., Khare P., 1994, ApJ, 428, 82
Steidel C. C., 1995, in Meylan G., ed., Proceedings of the ESO Workshop, QSO Absorption Lines. Springer-Verlag Berlin, Heidelberg New York, p. 139
Tinker J. L., Chen H.-W., 2008, ApJ, 679, 1218
Tumlinson J., Peeples M. S., Werk J. K., 2017, ARA&A, 55, 389
Tytler D. et al., 2009, MNRAS, 392, 1539
Wang Z., Xu H., Yang X., Jing Y., Wang K., Guo H., Dong F., He M., 2021, Sci. China Phys. Mech. Astron., 64, 289811
Zahedy F. S., Chen H.-W., Rauch M., Wilson M. L., Zabludoff A., 2016, MNRAS, 458, 2423
Zehavi I. et al., 2011, ApJ, 736, 59
Zhu G., Ménard B., 2013, ApJ, 770, 130

SUPPORTING INFORMATION

Supplementary data are available at *MNRAS* online.

sample_table.csv

Please note: Oxford University Press is not responsible for the content or functionality of any supporting materials supplied by the authors. Any queries (other than missing material) should be directed to the corresponding author for the article.

This paper has been typeset from a TEX/LATEX file prepared by the author.